THREE PROBLEMS IN THE LARGE–EDDY SIMULATION OF COMPLEX TURBULENT FLOWS

Krishnan Mahesh, Yucheng Hou and Pradeep Babu

Department of Aerospace Engineering & Mechanics
University of Minnesota
Minneapolis, MN 55455, USA
email: mahesh@aem.umn.edu

Keywords: compressible algorithm, discrete energy–conservation, near–wall modeling, rapid distortion theory, scalar mixing model, turbulent jet

Abstract. *This paper discusses: (i) an algorithm that addresses the problems posed by low Mach numbers and high Reynolds numbers in large–eddy simulation of compressible turbulent flows, (ii) the near–wall modeling problem for attached turbulent boundary layers, and (iii) a simple kinematic model that possibly explains why large–eddy simulation predicts turbulent mixing accurately, even though the viscous processes are not being represented.*

1 AN ALGORITHM FOR LARGE–EDDY SIMULATION OF COMPRESSIBLE TURBULENT FLOWS

1.1 Introduction

A key issue in turbulence simulation is ensuring robustness without the use of numerical dissipation. Considerable attention has been devoted to this problem for incompressible flows, where algorithms that discretely conserve kinetic energy have been found to be very successful in reliably performing large–eddy simulation (LES). However, the compressible equations do not conserve kinetic energy; energy is exchanged between kinetic and potential energy. Also, small Mach numbers result in the compressible equations becoming very stiff. A solution that addresses both problems is discussed below. The basic idea is that a robust algorithm for compressible turbulence may be derived by requiring that the discrete equations reduce to the incompressible equations at low Mach numbers, and that the discretization conserves kinetic energy in the inviscid incompressible limit. Hou & Mahesh (2005) discuss the approach in detail; this paper summarizes the results.

1.2 Governing equations

The governing equations are the compressible Navier–Stokes equations which are non–dimensionalized as follows:

$$\rho = \frac{\rho^d}{\rho_r}, \;\; u_i = \frac{u_i^d}{u_r}, \;\; t = \frac{t^d}{L/u_r}, \;\; \mu = \frac{\mu^d}{\mu_r},$$
$$p = \frac{p^d - p_r}{\rho_r {u_r}^2}, \;\; T = \frac{T^d}{T_r}, \;\; \text{and} \;\; M_r = \frac{u_r}{a_r} = \frac{u_r}{\sqrt{\gamma R T_r}}. \tag{1}$$

u_r, L, ρ_r, T_r are the reference velocity, length, density and temperature respectively. The reference pressure, $p_r = \rho_r R T_r$. Note that the pressure has been non–dimensionalized as $p = \frac{p^d - p_r}{\rho_r {u_r}^2}$. This yields the following non–dimensional equations:

$$\frac{\partial \rho}{\partial t} + \frac{\partial \rho u_j}{\partial x_j} = 0, \tag{2a}$$
$$\frac{\partial \rho u_i}{\partial t} + \frac{\partial \rho u_i u_j}{\partial x_j} = -\frac{\partial p}{\partial x_i} + \frac{1}{Re}\frac{\partial \tau_{ij}}{\partial x_j}, \tag{2b}$$
$$M_r^2 \left[\frac{\partial}{\partial t}\left(p + \frac{\gamma-1}{2}\rho u_i u_i \right) + \frac{\partial}{\partial x_j}\left(\gamma p + \frac{\gamma-1}{2}\rho u_i u_i \right) u_j \right] + \frac{\partial u_j}{\partial x_j}$$
$$= \frac{(\gamma-1)M_r^2}{Re}\frac{\partial \tau_{ij} u_i}{\partial x_j} + \frac{1}{RePr}\frac{\partial}{\partial x_j}\left(\frac{\mu \partial T}{\partial x_j} \right). \tag{2c}$$

The non–dimensional equation of state is:

$$\rho T = \gamma M_r^2 p + 1. \tag{3}$$

Note that as M_r tends to zero, the energy equation (2c) reduces to $\frac{\partial u_j}{\partial x_j} = \frac{1}{RePr}\frac{\partial}{\partial x_j}\left(\frac{\mu \partial T}{\partial x_j}\right)$. Along with the continuity equation, this shows that the velocity field is divergence–free if the density and temperature are constant. On the other hand, if the Boussinesque approximation is made, an advection–diffusion equation is obtained for temperature. The equation of state similarly reduces to $\rho T = 1$. The above non–dimensional equations therefore naturally yield the incompressible equations in the limit of very small Mach number. Also, all spatial derivatives in the above equations are in divergence form, and hence conservative. The above set of governing equations are therefore very attractive in that at high Mach numbers, they would yield the proper jump in variables across shock waves, and at very small Mach numbers, variations on the fast, acoustic time–scale would be projected out at time–steps larger than the acoustic time–scale. Bijl & Wesseling (1998) and Van der Heul et al. (2002) use a similar set of equations to obtain a staggered algorithm on structured grids for the Euler equations, and inviscid MHD equations respectively. While Bijl & Wesseling solve the energy equation in non–conservative form, a fully conservative energy equation is used by van der Heul et al (2002).

1.3 Discretization

The Cartesian velocities, pressure and density are colocated in space at the centroids of the control volumes. Also, density, pressure and temperature are staggered in time from velocity. This feature makes the discretization symmetric in space and time, and is essential to ensuring zero dissipation at finite time-steps. The face normal velocity is located at the face centers and denoted by v_N in this paper. At every time step, the velocity components u_i, and v_N are advanced from time t to $t+1$ and the thermodynamic variables, p, ρ and T are advanced from $t+\frac{1}{2}$ to $t+\frac{3}{2}$.

Integrating the governing equations over a control volume, and using Gauss' theorem to transform volume integrals into surface integrals yields the following discrete equations:

$$\frac{\rho_{cv}^{t+\frac{3}{2}} - \rho_{cv}^{t+\frac{1}{2}}}{\Delta t} + \frac{1}{V}\sum_{faces} \rho_{face}^{t+1} v_N^{t+1} A_{face} = 0. \tag{4}$$

$$\frac{g_{i,cv}^{t+1} - g_{i,cv}^{t}}{\Delta t} + \frac{1}{V}\sum_{faces} g_{i,face}^{t+\frac{1}{2}} v_N^{t+\frac{1}{2}} A_{face} = -\frac{\partial}{\partial x_i} p_{cv}^{t+\frac{1}{2}} + \frac{1}{Re}\frac{1}{V}\sum_{faces}\left(\tau_{ij}^{t+\frac{1}{2}}\right)_{face} N_j A_{face}. \tag{5}$$

Here, $g_i = \rho u_i$ denotes the momentum in the i direction and $(\tau_{ij})_{face}$ is the stress tensor at the face. N_j is the outward normal vector at the face. $p_{cv}^{t+\frac{1}{2}}$ is obtained by applying the trapezoidal rule to integrate the pressure–gradient term. The discrete energy equation is given by

$$M_r^2\left[\frac{\partial}{\partial t}\left(p_{cv} + \frac{\gamma-1}{2}\rho u_i u_i\right)^{t+\frac{1}{2}} + \frac{1}{V}\sum_{faces}\left(\gamma p_{cv} + \frac{\gamma-1}{2}\rho u_i u_i\right)_{face}^{t+\frac{1}{2}} \cdot v_N^{t+\frac{1}{2}} A_{face}\right]$$
$$+\frac{1}{V}\sum_{face} v_N^{t+\frac{1}{2}} A_{face} = \frac{(\gamma-1)M_r^2}{Re}\frac{1}{V}\sum_{faces}(\tau_{ij}u_i)_{face}^{t+\frac{1}{2}} N_j A_{face}$$
$$+\frac{1}{RePr}\frac{1}{V}\sum_{faces}\left(\mu\frac{\partial T^{t+\frac{1}{2}}}{\partial N}\right) A_{face}. \tag{6}$$

The central differences in time and space make the algorithm second order on regular grids. Also, the algorithm is fully implicit, and hence not limited by viscous, convective or acoustic stability limits. The discrete energy equation shows that M_r and Δt determine whether high frequency acoustics are captured in a time–accurate manner. At small Mach numbers, Δt of the order of M_r^2 allows acoustic waves to be represented in a time–accurate manner. When high frequency acoustics are not of physical importance, the Δt may be of the order of the convective time–scale, and the energy–equation discretely projects out acoustic effects and yields zero–divergence for the velocity field.

A pressure–correction method is used to solve the above equations. A notable feature is that the face–normal velocities are projected to satisfy a constraint on the divergence that is determined by the energy equation. This is

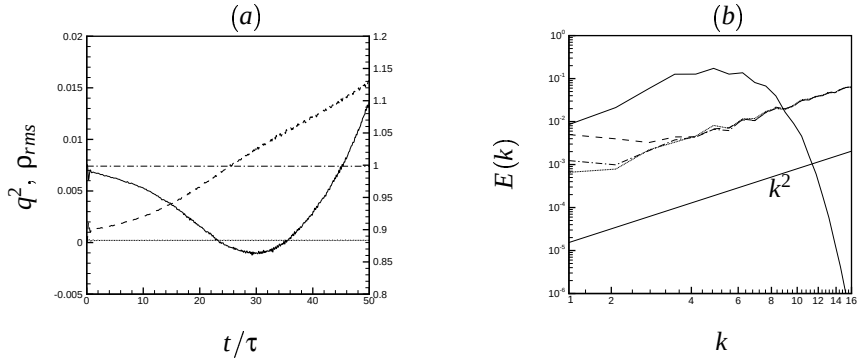

Figure 1: Long–time evolution of inviscid, isotropic, compressible turbulence. (a) ——— turbulence kinetic energy at $M_t = 0.4$, - - - - rms density at $M_t = 0.4$, —·— turbulence kinetic energy at $M_t = 0.01$, ····· rms density at $M_t = 0.01$. The range of kinetic energy is shown on the right of the plot, while the left of the plot shows the range of rms density. (b) Three–dimensional energy ($E(k)$) spectra as a function of time for inviscid, isotropic, compressible turbulence ($M_t = 0.01$. The energy spectrum is normalized by the initial value of q^2 ——— $t/\tau = 0$, - - - - $t/\tau = 5$, —·— $t/\tau = 10$, ····· $t/\tau = 70$.

in contrast to most approaches that project the momentum to be constrained by the continuity equation. A result of using the energy equation to project the velocity is that at small Mach number, the projection step ensures that the velocity field is discretely divergence–free. Also as will be seen below, there is no odd–even decoupling in the incompressible limit. An iterative approach is used to solve the continuity, momentum and energy equations. Let k denote an iteration level in an outer loop which seeks to advance the the velocities from t to $t+1$ and pressure, temperature and density from $t+\frac{1}{2}$ to $t+\frac{3}{2}$. The discrete energy equation yields an equation for the pressure correction, δp. The solution procedure is as follows.

1. Initialize the outer loop; i.e.

$$u_i^{t+1,0} = u_i^t,\ \rho^{t+\frac{3}{2},0} = \rho^{t+\frac{1}{2}},\ T^{t+\frac{3}{2},0} = T^{t+\frac{1}{2}},\ v_N^{t+1} = v_N^t.$$

2. Advance the continuity equation to get $\rho^{t+\frac{3}{2},k+1}$ by using the face normal velocity $v_N^{t+1,k}$.

3. Advance the momentum predictor equation to get a provisional value of g_i^* by using pressure and velocity at current iteration step.

4. Obtain velocities at the control volume centers using $u_i^* = g_i^*/\rho^{t+1,k+1}$ where $\rho^{t+1,k+1} = \left(\rho^{t+3/2,k+1} + \rho^{t+1/2}\right)/2$. Interpolate u_i^* to obtain v_N^* at the faces.

5. Solve the pressure correction equation to get δp.

6. Update the pressure, momentum and the velocities at center of the control volumes, and update the face normal velocity using the pressure correction.

7. Check convergence for the pressure correction, density and momentum between outer loop iterations.

1.4 Results

The algorithm is applied to simulate homogeneous, decaying isotropic turbulence on a very coarse grid without a subgrid model. This problem poses a severe test of the capability of the algorithm to ensure robustness at high Reynolds numbers without numerical dissipation. The initial fluctuation Mach number $M_t = q/a$ and turbulent Reynolds number, $Re_\lambda = \frac{u_{rms}\lambda}{\nu}$. Here, $q = \sqrt{u_i' u_i'}$, $a = \sqrt{\gamma R T_0}$ is the mean speed of sound, and λ denotes the initial Taylor microscale. Simulations are performed for compressible ($M_t = 0.4$), and nearly incompressible ($M_t = 0.01$) conditions. Results are shown for $R_\lambda = \infty$; (i.e. inviscid). The domain is $(2\pi)^3$, and the computational grid has 32 points in each direction. The time–step is fixed at 0.025 τ where τ is an 'eddy–turnover' time–scale which is equal to the initial value of λ/u_{rms}. Note that no subgrid model is used for this simulation. Figure $1(a)$ shows the solution over a long time. Note that at $M_t = 0.4$, the solution is stable up to about 30τ, following which the kinetic energy and density fluctuations increase rapidly. This behavior is due to the formation of shock waves in the domain. In contrast, the $M_t = 0.01$ flow maintains its initial kinetic energy over this length of time. Figure $1(b)$ shows three–dimensional spectra of the turbulence kinetic energy for the $M_t = 0.01$ flow. Note that the nearly

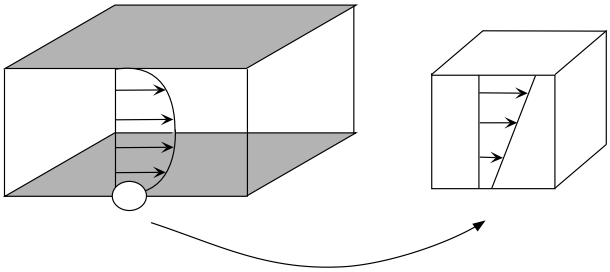

Figure 2: Schematic of the problem.

incompressible flow exhibits equipartition; i.e. its spectrum at long times varies as k^2. These results therefore show that the algorithm is stable even in the inviscid limit on the convective time-scale, and is unstable only when shock waves form. This behavior is in contrast to other commonly used non–dissipative schemes which become unstable at very short times even at very low Mach numbers; i.e. they are unstable on the convective time–scale ($t/\tau \sim 1$) at high Reynolds numbers (e.g. see figure 11 in Nagarajan et al 2003). Dissipative methods would cause the solution to decay even in the inviscid limit.

1.5 Summary

The algorithm addresses the problems caused by low Mach numbers and under–resolved high Reynolds numbers without numerical dissipation. It colocates variables in space to allow easy extension to unstructured grids, and discretely conserves mass, momentum and total energy. The discrete divergence is constrained by the energy equation. As a result, the discrete equations analytically reduce to the incompressible equations at very low Mach number. The algorithm discretely conserves kinetic energy in the incompressible inviscid limit, and is robust for inviscid compressible turbulence on the convective time-scale. These properties make it well-suited for DNS/LES of compressible turbulent flows. A limitation, which needs to be overcome in the future is lack of shock–capturing ability.

2 THE NEAR–WALL MODELING PROBLEM

2.1 Introduction

Large–eddy simulations of attached boundary layers at high Reynolds numbers require very fine near–wall resolution when the LES equations are integrated down to the wall. We consider the question of whether common subgrid models are modeling the dominant physical/numerical effect of the subgrid scales in the inner–layer region. Most subgrid models are required to model the net non–linear transfer of energy from the resolved scales to the subgrid scales. However, Kline et al. (1967), Uzkan & Reynolds (1967), and Lee et al. (1990) suggest that streaks, which dominate the near–wall region, are produced by the *linear* mechanism of rapid straining of turbulent fluctuations. Lee et al. in particular, establish a close connection between turbulence in the viscous sub–layer, and homogeneous turbulence that is sheared at very high shear–rates. They also show that the evolution of rapidly sheared homogeneous turbulence is well described by linear rapid distortion theory (RDT) and that the RDT can reasonably predict the Reynolds stress anisotropy and structural features of near–wall turbulence.

We therefore consider the possibility that the errors involved when numerically solving the RDT equations on a coarse mesh might correspond to the errors in the near–wall region on coarse meshes. The discretized RDT equations, thus obtained, can be solved analytically using the notion of 'modified wave–number'. The RDT equations are then analyzed to explain the observed trends.

2.2 Inviscid Rapid distortion theory

Figure 2 shows a schematic of the problem where initially isotropic turbulence is subjected to mean shear. The rate of shear is assumed rapid as compared to characteristic time-scales of the turbulence. The mean velocity for homogeneous shear is

$$U_1 = Sx_2, \quad U_2 = U_3 = 0. \tag{7}$$

and the corresponding coordinate transformation which yields constant coefficient equations (Rogallo 1981) is $\xi_1 = x_1 - Stx_2, \quad \xi_2 = x_2, \quad \xi_3 = x_3, \quad \tau = t$. The coordinate transformation yields linear, constant–coefficient equations which are then solved using conventional Fourier representation. Knowledge of the Fourier coefficients

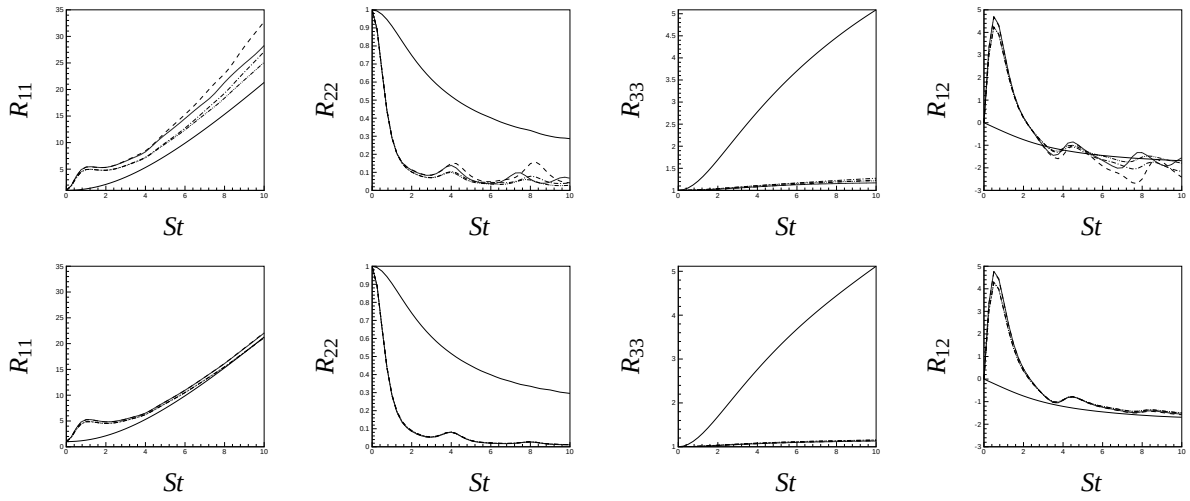

Figure 3: The evolution of the Reynolds stresses (normalized by the initial value of $R_{ii}/3$) as a function of grid resolution when the RDT equations are numerically solved. The upper and lower rows correspond to the second-order central difference scheme, and Fourier derivatives respectively. The initial $E(k) \sim k^{-2}$. ——— Exact, - - - - $16 \times 128 \times 16$ mesh, —·— $32 \times 128 \times 32$ mesh, ····· $16 \times 16 \times 16$ mesh, —··— $32 \times 32 \times 32$ mesh.

enables computation of the energy spectrum tensor which is then integrated over all wavenumbers to determine the Reynolds stresses. The wavenumbers vary continuously from $-\infty$ to $+\infty$ in an analytical representation of the turbulent field. Two important differences arise when the same problem is numerically solved. First, finite spatial resolution implies that the wavenumbers are finite, and given by $k_i = 2\pi j/L$, where j varies from $-N/2$ to $N/2-1$. Here, N denotes the number of grid points, and L denotes the domain size in the i^{th} direction. Second, discretization error results in the spatial derivatives in the linear equation not being correctly represented. Both factors result in the evolution of the numerical solution being different from the analytical solution.

An analytical solution to the discrete RDT equations can be obtained. The solution is identical to the classical analytical solutions (e.g. Townsend 1976, Rogers 1991) with the exception that wavenumbers in the analytical solutions are replaced by the modified wavenumber (see Moin 2001 for a discussion of modified wave–numbers). Note that the solution is completely general in the choice of numerical scheme.

2.3 Results

Two initial spectra are considered in this paper, $E(k) \sim k^{-2}$ and $E(k) \sim (k/k_0)^4 \mathrm{e}^{-2(k/k_0)^2}$. The first choice of spectrum corresponds to the situation where the grid is so coarse that even the largest energy–containing motions are not resolved. Even a Fourier method would yield incorrect solutions under these conditions. When direct numerical simulation is performed in a channel, the minimal channel notion of Jimenez & Moin (1991) suggests that the essential dynamics of the near-wall region and outer region can be though of as being independent and so resolved small scale turbulence near the wall is rapidly sheared. But when the near–wall region is severely under–resolved, outer layer motions that are larger than the near-wall region will experience near-wall shear. The k^{-2} spectrum attempts to model this situation. The second choice of spectrum corresponds to the situation where the energy–containing motions are resolved by the grid. A Fourier method would be expected to yield reasonable results under these conditions while less accurate numerical schemes would show the effects of discretization error.

Lee et al. (1990) establish the relation between homogeneous shear and near–wall turbulence using statistics at $St = 8$. In assessing the impact of numerical error, this paper therefore uses the RDT solution at $St = 8$.

2.4 k^{-2} initial spectrum

Figure 3 shows the effect of truncation error when the RDT equations are numerically solved. The initial three–dimensional energy spectrum, $E(k)$ varies as k^{-2}. The RDT equations are solved using a second–order central difference scheme; i.e. $k'_\alpha = \sin k_\alpha \Delta_\alpha / \Delta_\alpha$. The finite–difference results are contrasted to those obtained using Fourier differentiation to isolate the effects of discretization error and truncation. Four different grids are considered – $16 \times 128 \times 16$, $32 \times 128 \times 32$, $16 \times 16 \times 16$, and $32 \times 32 \times 32$, respectively. The resolution of 128 in the y direction is chosen to approximate the channel simulation where the near–wall normal direction is nearly resolved ($\Delta y^+ \leq 1$), while vertical resolutions of 16 and 32 assume that the corresponding channel simulation is not resolved in the near–wall direction.

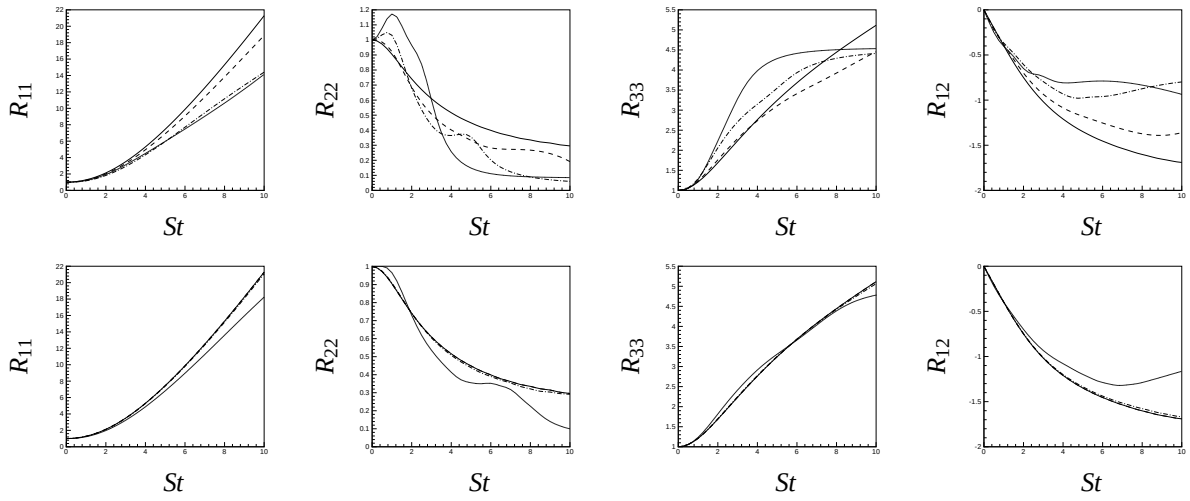

Figure 4: The evolution of the Reynolds stresses (normalized by the initial value of $R_{ii}/3$) as a function of grid resolution when the RDT equations are numerically solved. The upper and lower rows correspond to the second-order central difference scheme, and Fourier derivatives respectively. The initial $E(k) \sim (k/k_0)^4 e^{-2(k/k_0)^2}$ where $k_0 = 10$. ——— Exact, – – – – $64 \times 64 \times 64$ mesh, —·— $32 \times 32 \times 32$ mesh, ····· $16 \times 16 \times 16$ mesh.

Around $St = 8$, the streamwise intensities are higher, while the vertical and spanwise intensities are smaller than their actual values. The Reynolds shear stress is closer to the exact solution than the intensities. While it does not show smaller magnitudes at all St, it oscillates about the exact solution at longer times, and is smaller in magnitude for small St. Fourier differentiation yields essentially the same results as the finite–difference scheme for R_{22} and R_{33}, although R_{11} and R_{12} are closer to the exact solution. This behavior is in contrast to that described below when the initial spectrum is resolved on the computational grid, and is explained in section 2.6.

2.5 Resolved initial spectrum

Figure 4 shows results from RDT computations where the initial spectrum corresponds to turbulence that is resolved on the computational grid prior to being sheared. The initial $E(k) \sim (k/k_0)^4 e^{-2(k/k_0)^2}$. Here k_0 is the wavenumber at which the spectrum peaks, and is chosen to be 10. Grids of size, $16^3, 32^3$ and 64^3 are considered. Since the turbulence is initially resolved, noticeable difference is observed between results obtained using a Fourier spectral scheme, and the second order finite difference scheme. Note that Fourier differentiation shows good agreement with analytical solution on the 32^3 and 64^3 grids for which the peak in the initial spectrum is less than the grid cut–off wavenumber ($k = 32$ and 16 respectively). Deviation from the analytical solution is only seen for the 16^3 grid for which the cut–off wavenumber ($k = 8$) is less than the peak in the spectrum. In contrast, the finite–difference solutions deviate from the exact solution at all resolutions. Note that R_{22}, R_{33} and R_{12} are all less in magnitude than their exact values. However, R_{11} is now less in magnitude than the exact solution. This behavior is in contrast to that observed when the initial spectrum was not resolved, and is a result of the finite–difference scheme representing the smallest resolved scales inaccurately. The modified wavenumber shows that differencing error in the finite–difference scheme is significant beyond $k\Delta \sim 1$. The peak in the initial spectrum corresponds to $k_0\Delta = k_0 2\pi/N$ where N is the number of grid points in each direction. The $16^3, 32^3$ and 64^3 grids yields values of $k_0\Delta$ of 3.93 (unresolved), 1.96 and 0.98 respectively. The resulting truncation error has the effect of ignoring the energetic scales in the initial condition, the growth in energy in those scales due to mean shear is not represented, and the net result is an underprediction of the Reynolds stresses.

2.6 An explanation

The RDT equations show that the only variable being spatially differentiated is the fluctuating pressure. Truncation error would therefore entirely result from errors in approximating the spatial derivatives in pressure, and then projecting the velocity field to ensure the divergence–free condition. Note that this error includes the effects of both excluding high wavenumber modes, and discretization error in differentiating the resolved modes. The analytical derivatives are exact for the resolved wavenumbers when Fourier methods are used, but exclusion of high wavenumber information implies that the derivatives in physical space are incorrect. Using finite–difference or finite–volume schemes to compute the spatial derivatives increases the error since even the resolved wavenumbers are not differentiated exactly.

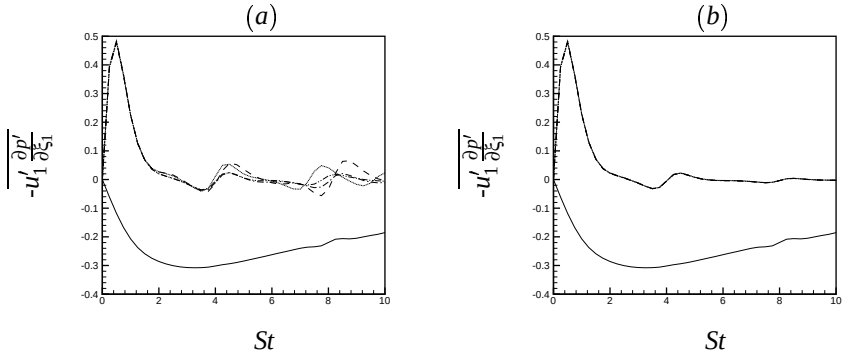

Figure 5: The pressure-strain correlation (normalized by the initial value of $SR_{ii}/3$) in the R_{11} equation as a function of grid resolution when the RDT equations are numerically solved using (a) : the second-order central difference scheme, (b): Fourier differentiation. $E(k) \sim k^{-2}$ initially. ——— Exact, - - - - $16 \times 128 \times 16$ mesh, —·— $32 \times 128 \times 32$ mesh, ····· $16 \times 16 \times 16$ mesh, —··— $32 \times 32 \times 32$ mesh.

The evolution equations for the Reynolds stresses in the RDT limit allow further clarification. We have

$$\begin{aligned} \frac{\mathrm{d}}{\mathrm{dt}} R_{11} &= -SR_{12} - \overline{u_1' \frac{\partial p'}{\partial \xi_1}}, \\ \frac{\mathrm{d}}{\mathrm{dt}} R_{22} &= -\overline{u_2' \frac{\partial p'}{\partial \xi_2}} + St\ \overline{u_2' \frac{\partial p'}{\partial \xi_1}}, \quad \text{and} \\ \frac{\mathrm{d}}{\mathrm{dt}} R_{33} &= -\overline{u_3' \frac{\partial p'}{\partial \xi_3}}. \end{aligned} \tag{8}$$

The Reynolds shear stress, R_{12} combines with mean shear to 'produce' R_{11}. The pressure–strain correlation, $\overline{u_1' \frac{\partial p'}{\partial \xi_1}}$ acts to redistribute energy from R_{11} to the other two components.The RDT results show that R_{11} is higher than expected, although R_{12} is smaller or even equal to the correct value. In other words, R_{11} is *higher* although the production term is *smaller*. This is only possible if the pressure–strain correlation is not large enough. Figure 5 shows the pressure-strain correlation in the R_{11} equation in the RDT limit. The pressure–strain term is indeed smaller at coarse resolutions for all resolutions considered.

Suppression of the transfer from u_1' to the other components may be considered a result of constraining the velocity field to be divergence–free in the presence of truncation error. Each of the individual derivatives, $\partial u_\alpha / \partial x_\alpha$ is incorrect due to truncation and discretization. The sum of the three gradients is still constrained to be zero. In terms of the Reynolds stresses, this error shows up in the pressure–strain correlation.

2.7 Summary

This suggests that, near the wall, it is probably more important to account for the effect of the subgrid scales on the non–local effects of pressure than it is to model their nonlinear effects due to advection. One way to achieve this might be to use the equivalent of Reynolds stress modeling for LES, where the pressure–strain correlation would be explicitly modeled. Another possibility is to retain presently used models for the subgrid stress, but allow the velocity field to have a finite–divergence. This divergence could be modeled in a variety of ways. e.g. $\sim C\Delta_i \frac{\partial \overline{u}_i}{\partial x_j \partial x_j}$ where C is a constant that could be obtained from direct numerical simulation (DNS) data, or obtained dynamically, and Δ_j denotes the filter width in each coordinate direction, which ensures that the velocity field is divergence–free in the DNS limit.

3 PASSIVE SCALAR MIXING

3.1 Introduction

There is reasonable evidence to suggest that large–eddy simulation yields better predictions than RANS–based approaches for turbulent mixing, and is therefore more suited to applications such as turbulent combustion. However, one objection that is commonly raised, is that turbulent mixing requires molecular mixing at the diffusive scales, and therefore LES, which does not directly represent the diffusive scales should not yield accurate predictions. This paper attempts to answer this concern by proposing a kinematic model for the scalar fluctuations, which predicts the fluctuations in scalar without detailed knowledge of the diffusive processes. The model is motivated

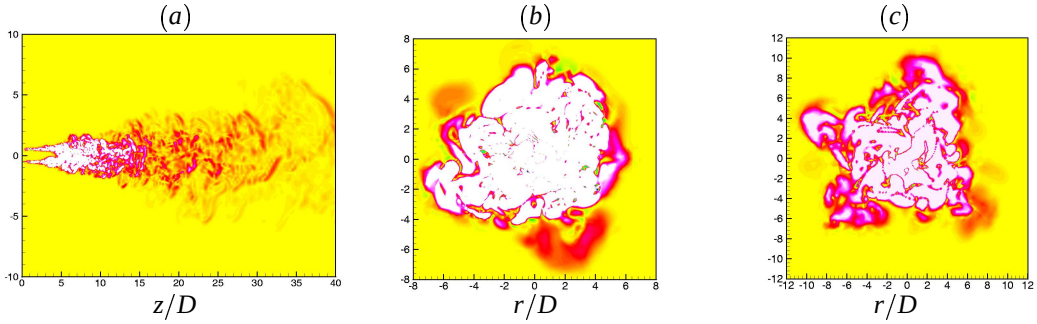

Figure 6: Instantaneous contours of Ψ. (a): radial cross–section, (b): axial cross–section at $z/D = 30$, and (c): axial cross–section at $z/D = 45$. Color scheme: white denotes convection–dominated regions, and the dark regions correspond to diffusion–dominated regions.

by observations from a direct numerical simulation of scalar mixing in a turbulent jet. Babu & Mahesh (2005) give a detailed description; this paper summarizes their results.

3.2 Results from DNS

Direct numerical simulation of passive scalar transport in a spatially evolving turbulent jet was performed at Reynolds number of 2400 and Schmidt number of unity. Good comparison with experimental data was obtained for the mean velocity, mean scalar concentration, and fluctuations of velocity and scalar (Babu & Mahesh 2005).

In passive scalar mixing, viscous processes are commonly assumed to be restricted to very thin regions or scalar fronts. Experimental measurements of scalar dissipation in the interior of turbulent jets seem to have influenced this notion. However, a more direct estimate of viscous processes is provided by analysis of the instantaneous diffusion and convection terms in the passive scalar equation. A variable Ψ is introduced, which is the difference between the absolute values of the convection and diffusion terms,

$$\Psi = \underbrace{\left| \frac{\partial (c u_j)}{\partial x_j} \right|}_{\text{Convection}} - \underbrace{\left| \frac{1}{Re\, Sc} \frac{\partial^2 c}{\partial x_j \partial x_j} \right|}_{\text{Viscous diffusion}} \tag{9}$$

where c and u_j denote the scalar concentration and velocity respectively. Small absolute values of Ψ therefore denote regions where the diffusion term is as significant as convection, and negative values of Ψ denote regions where viscous diffusion is dominant. Contours of Ψ are shown in figure 6. Note that the regions where diffusion is important, thicken radially outward, and become 'brush–like' near the edges. Statistics of Ψ were gathered, and show the same trends as the instantaneous contours. This behavior may be explained by noting that the residence time of fluid increases near the jet edge due to very low levels of turbulence there. The implication of this observation is that the jet will be more sensitive to Reynolds number at its outer edges than it would at the centerline. This notion has a parallel in boundary layers where the 'viscous superlayer' at the boundary layer edge makes the wake–parameter dependent on Reynolds number for $Re_\theta < 5000$ (Huffman & Bradshaw 1972). However, an important difference is that the velocity field in the viscous superlayer is highly intermittent while the outer 'brush–like' regions are fairly quiescent. A simple kinematic model based on these ideas, is proposed below.

3.3 Kinematic model for scalar fluctuations

The Reynolds number dependence of scalar fluctuations in turbulent jets is summarized by Dimotakis (2000, figure 6 of his paper, reproduced in figure 8b), who shows $c_{\text{rms}}/\overline{c}$ at the centerline as a function of jet Reynolds number, for liquid–phase and gas–phase jets. The data show that $c_{\text{rms}}/\overline{c}$ at the jet centerline decreases with increasing Reynolds number, and reaches an asymptotic value at sufficiently high Reynolds number. Gas phase jets are observed to be less sensitive to Reynolds number than liquid phase jets, over the range of Reynolds numbers shown.

A simple kinematic model is proposed below, that predicts the experimentally observed variation of scalar fluctuations at the jet centerline with Reynolds number and Schmidt numbers. The model is also used to show that the radial variation of scalar fluctuations in turbulent jets may be interpreted using the same arguments. The model assumes that scalar fluctuations at a fixed location in the jet result from the oscillation of scalar fronts, whose thickness depends on Reynolds number, Schmidt number, and radial position in the jet, and whose oscillation amplitude depends on the level of turbulent fluctuations. The main idea behind the model is that the oscillation

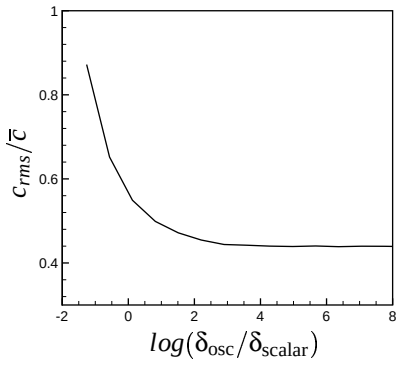

Figure 7: Predicted values of scaled scalar intensity ($c_{max}/\overline{c}$ = 1) plotted against the ratio of the oscillation amplitude of scalar fronts to their thickness.

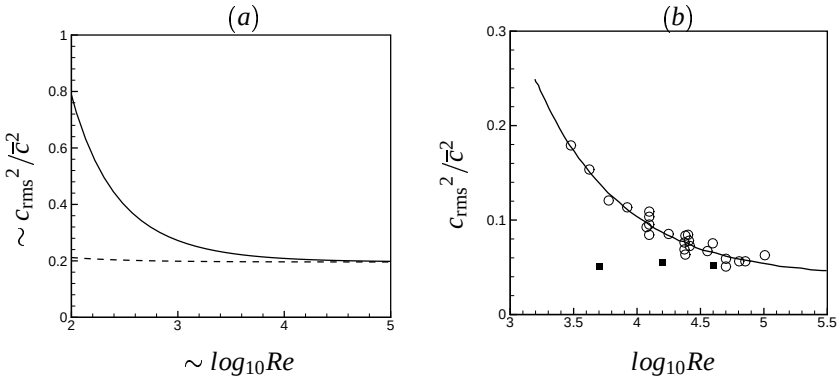

Figure 8: Comparison of model prediction to experiments. Note that the axes in the model prediction are proportional to the Reynolds number and scalar intensity. (a): Model, (———) liquid phase and (- - - -) gas phase jets. (b): experimental data from Dimotakis (2000). (○) water jet (Miller & Dimotakis 1991), (■) air jet (Dowling & Dimotakis 1990) and (———) suggested data fit by Dimotakis (2000) for water jets.

of sharp gradients produces high levels of fluctuations. The scalar concentration in the vicinity of a measurement location in the jet is assumed to vary as follows. The fluctuations about the local mean ($\overline{c}$) are represented by fronts of thickness, δ_{scalar}, which are oscillated with amplitude δ_{osc}. Consider

$$\begin{aligned} g(x) &= \frac{c_{max}}{\overline{c}} \sin\left(\frac{\pi x}{\delta_{scalar}}\right) \text{ if } \sin\left(\frac{\pi x}{\delta_{scalar}}\right) > 0, \\ &= 0 \text{ if } \sin\left(\frac{\pi x}{\delta_{scalar}}\right) \leq 0. \end{aligned} \tag{10}$$

The domain is assumed to be equal to length 2π for convenience. Each period of the sine function in $g(x)$, or equivalently, each blip in $g(x)$ is assigned an equal probability of being positive or negative. Furthermore each blip is randomly translated over a distance bounded by $\pm\delta_{osc}$. The problem is statistically homogeneous, and so statistics are computed by averaging over x and time. Note that the scalar profile is completely described by the non–dimensional parameters, $c_{max}/\overline{c}$ and $\delta_{osc}/\delta_{scalar}$. It is readily seen that $c_{max}/\overline{c}$ affects the absolute levels of scalar intensities, but not their variation with $\delta_{osc}/\delta_{scalar}$.

3.3.1 Effect of Reynolds and Schmidt numbers

The parameter, $\delta_{osc}/\delta_{scalar}$ represents the ratio of the amplitude of oscillation of scalar fronts to their thickness. Its value will therefore depend on jet Reynolds number, Schmidt number, and radial position. As the Reynolds number increases, the thickness of the scalar fronts is expected to decrease, which implies that $\delta_{osc}/\delta_{scalar}$ increases. Similarly, increasing the Schmidt number will decrease the thickness of the scalar fronts, and therefore increase the ratio, $\delta_{osc}/\delta_{scalar}$. Recall that the thickness of the regions where diffusion is important in the jet, increases with increasing radius. Also, the turbulence levels decrease with increasing radius. This means that $\delta_{osc}/\delta_{scalar}$ will decrease away from the jet centerline towards the edges. This dependence can be represented as

$$\frac{\delta_{osc}}{\delta_{scalar}} \sim \frac{Re^n \cdot Sc^p}{r^m}, \tag{11}$$

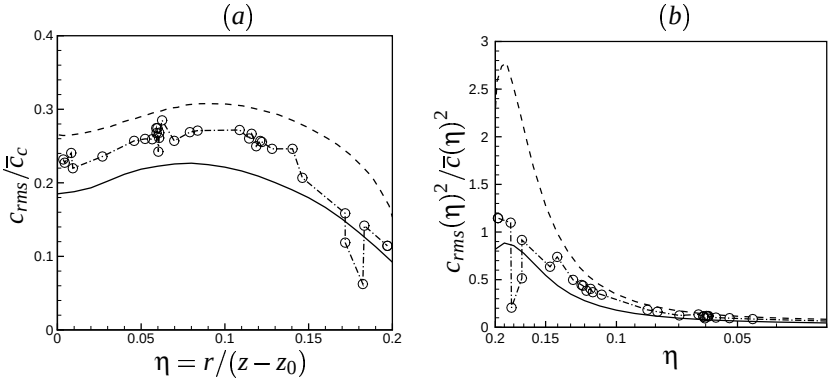

Figure 9: rms value of fluctuations in scalar concentration normalized with (a): mean scalar concentration at jet centerline, (b): mean local scalar concentration. Note: x–axis in (b) is plotted in inverse log scale. (– – – – , $Re = 5000, Sc \sim 600$) Dahm & Dimotakis (1987), (— – — ∘ , $Re = 5000, Sc = 1.0$) Dowling & Dimotakis (1990) and (——— , $Re = 2400, Sc = 1.0$) present DNS.

where m, n and p are positive.

Figure 7 shows the variation of $c_{\rm rms}/\overline{c}$ with varying $\delta_{\rm osc}/\delta_{\rm scalar}$. The parameter, $c_{\rm max}/\overline{c}$ was set equal to one, while $\delta_{\rm osc}/\delta_{\rm scalar}$ was varied from 3×10^{-3} to 10^3. Note that the intensity of the scalar fluctuations decreases, and asymptotes to a constant value for sufficiently high values of the ratio $\delta_{\rm osc}/\delta_{\rm scalar}$. This behavior is used below to explain the effect of the Reynolds number, Schmidt number and radial position in the jet.

At fixed radial distance and Schmidt number, equation 11 shows that $\delta_{\rm osc}/\delta_{\rm scalar} \sim Re^n$. Increasing Re is therefore equivalent to increasing the magnitude of $\delta_{\rm osc}/\delta_{\rm scalar}$, which according to figure 7 results in the scalar intensity decreasing and reaching a constant value at sufficiently high Reynolds numbers.

The experimental data in figure 8(b) show two trends with varying Schmidt number: gas jets appear less sensitive to Reynolds number than liquid jets, and at fixed Reynolds number, gas jets have lower values of scalar intensity. These trends are explained as follows. Assuming that the Schmidt numbers of water and gas jets are 10^3 and 1 respectively, equation 11 shows that at a fixed location r,

$$\begin{aligned} \frac{\delta_{\rm osc}}{\delta_{\rm scalar}} &\sim 10^{3p}\, Re^n \text{ for water jets} \\ &\sim Re^n \text{ for gas jets.} \end{aligned} \tag{12}$$

A finite change in Reynolds number therefore yields a much smaller change in the value of $\delta_{\rm osc}/\delta_{\rm scalar}$ for gas jets. Since the model predicts that scalar intensities depend on $\delta_{\rm osc}/\delta_{\rm scalar}$, this behavior will result in gas jets being less sensitive to Reynolds number than liquid jets.

Recall that the values of scalar intensity predicted by the model are scaled by the parameter, $c_{\rm max}/\overline{c}$. The reduced intensities in gas jets at fixed Reynolds numbers can be explained by noting that instantaneous scalar fronts in gas jets are different from those in liquid jets. It is known from experiment (e.g. Dahm & Dimotakis 1987, van Cruyningen et al. 1990, Dowling & Dimotakis 1990) that liquid jets entrain free–stream fluid to the jet centerline at low Reynolds numbers, but not at high Reynolds numbers. Gas jets on the other hand exhibit increased effects of diffusion due to which free–stream fluid is not observed at the jet centerline at low or high Reynolds numbers. This suggests that the peak value inside scalar fronts for gas jets would be less than that for liquid jets i.e. $c_{\rm max}/\overline{c}$ varies as Sc^α/Re^β. This results in gas phase jets having lower levels of scalar intensity than liquid jets at the same Reynolds number. It is apparent that this effect weakens at higher Reynolds numbers due to the $1/Re^\beta$ term.

Figure 8(a) shows model predictions for scaled scalar intensity, plotted in the same manner as the experimental data compiled by Dimotakis (2000) in 8(b). The model predictions require knowledge of the exponents for Reynolds number (n, β) and Schmidt number (p, β). These exponents are obtained from experimental measurements by Buch & Dahm (1998) and Su & Clemens (2003) who show that the thickness of fronts of high scalar dissipation varies as $\delta Re_\delta^{-3/4} Sc^{-1/2}$ where δ, Re_δ and Sc denote the outer–scale thickness, outer–scale Reynolds number and Schmidt number respectively. The Reynolds number exponents are therefore assumed to be equal to 3/4 and the Schmidt number exponents are assumed to be equal to 1/2 in obtaining figure 8(a). Note that the scaled scalar intensities display the same trends as the experimental data.

3.4 Effect of radial distance

Figure 9a shows scalar fluctuations non–dimensionalized with mean local centerline value, and plotted against the self–similarity variable $\eta = r/(z - z_0)$. The radial variation of scalar fluctuations can also be interpreted in terms of $\delta_{osc}/\delta_{scalar}$. At fixed *Re*, equation 11 yields, $\delta_{osc}/\delta_{scalar} \sim Sc^p/r^m$. Also, the model predictions are for c_{rms} normalized by the local value of $\overline{c}$. Equation 11 implies that

$$log(\delta_{osc}/\delta_{scalar}) \sim m \cdot log(\frac{1}{r + r_0}) + p \cdot log(Sc) \tag{13}$$

where r_0 prevents the singularity at $r = 0$. In logarithmic coordinates, $\delta_{osc}/\delta_{scalar}$ is therefore equivalent to $1/\eta$. Figure 9b shows the same data as in figure 9a, but non–dimensionalized with the *local* mean scalar value, and plotted against $1/\eta$. Note that the observed trends are similar to that predicted by the model in figure 7. Also, note that the effect of Schmidt number is the same as that discussed in the preceding section, and is more pronounced near the edges of the jet.

3.5 Summary

It is significant that the kinematic model makes no assumption about the diffusive processes inside the scalar fronts; it only requires that the variation of their thickness be represented. The model therefore suggests an explanation for the success of methods such as large–eddy simulation in predicting scalar mixing. Large–eddy simulation, by definition does not represent viscous dissipation; it only captures large–scale convective motions. According to the model, any modeling approach which accurately captures the energy–containing convective motions, and the approximate thickness of the scalar fronts will yield good predictions for the scalar field. Furthermore, predictions in gas–phase flows, or high Reynolds number flows are likely to be easier than those in liquid phase, low Reynolds number flows, given the significantly weaker dependence of gas phase scalar fluctuations on Reynolds number.

Acknowledgments

This work was supported by the the Air Force Office of Scientific Research under grant/contract FA9550-04-1-0341, Department of Energy through the Stanford ASC Alliance Program, and the Office of Naval Research under Grant N00014-02-1-0978. Computing time was provided by the Minnesota Supercomputing Institute, San Diego Supercomputer Center and National Center for Supercomputing Applications.

References

[1] Babu, P. & Mahesh, K., 2005, DNS and modeling of passive scalar mixing in turbulent jets. Submitted to *J. Fluid Mech.*

[2] Bijl, H. & Wesseling, P., 1998, A unified method for computing incompressible and compressible flows in boundary-fitted coordinates. *J. Comput. Phys.*, **141:** 153–173.

[3] Buch, K. A. & Dahm, W. J. A., 1998, Experimental study of the fine-scale structure of conserved scalar mixing in turbulent flows. Part 2. Sc $\sim$ 1. *J. Fluid Mech.* **364:** 1–29.

[4] Dahm, W. J. A. & Dimotakis, P. E., 1987, Measurements of entrainment and mixing in turbulent jets. *AIAA J.* **25:** 1216–1223.

[5] Dimotakis, P. E., 2000, Mixing transition in turbulent flows. *J. Fluid Mech.* **409:** 69–98.

[6] Dowling, D. R. & Dimotakis, P. E., 1990, Similarity of the concentration field of gas–phase turbulent jets. *J. Fluid Mech.* **218:** 109–141.

[7] Hou, Y. & Mahesh,K., 2005, A robust colocated implicit algorithm for direct numerical simulation of compressible turbulent flows, *J. Comput. Phys.*, **205(1):** 205–221.

[8] Huffman, G. D. & Bradshaw, P., 1972, A note on Von Kármán's constant in low Reynolds number turbulent flows. *J. Fluid. Mech.* **53:** 45–60.

[9] Jimenez, J. & Moin, P., 1991, The minimal flow unit in near–wall turbulence. *J. Fluid Mech.*, **225:** 213–240.

[10] Kline, S.J., Reynolds, W.C., Schraub, F.A. & Rundstadler, P.W., 1967, The structure of turbulent boundary layers. *J. Fluid Mech.*, **30:** 741–773.

[11] Lee, M.J., Kim, J. & Moin, P., 1990, Structure of turbulence at high shear rate. *J. Fluid Mech.* **216:** 561–583.

[12] Moin, P., 2001, Fundamentals of engineering numerical analysis. *Cambridge University Press*.

[13] Nagarajan, S., Lele, S.K. & Ferziger, J. H., 2003, A robust high-order compact method for large eddy simulation. *J. Comput. Phys.* **191:** 392–419.

[14] Rogallo, R.S., 1981, Numerical experiments in homogeneous turbulence. *NASA Tech. Mem.* 81315.

[15] Rogers, M.M., 1991, The structure of a passive scalar field with a uniform mean gradient in rapidly sheared homogeneous turbulence. *Phys. Fluids A*, **3**, 144–154.

[16] Su, L. K. & Clemens, N. T., 2003, The structure of fine–scale scalar mixing in gas–phase planar turbulent jets. *J. Fluid Mech.* **488:** 1–29.

[17] Townsend, A.A., 1976, The structure of turbulent shear flow. (2nd edn.) Cambridge University Press, Cambridge.

[18] Uzkan, T. & Reynolds, W.C., 1967, A shear-free turbulent boundary layer. *J. Fluid Mech.*, **28:** 803–821.

[19] van Cruyningen, I., Lozano, A. & Hanson, R. K., 1990, Quantitative imaging of concentration by planar laser–induced fluorescence. *Exp. Fluids* **10:** 41–49.

[20] Van der Heul, D.R., Vuik, C. & Wesseling, P., 2002, A conservative pressure-correction method for the Euler and ideal MHD equations at all speed. *Intnl. J. Num. Methods Fluids*, **40:** 521–529.